The Meteoritical Society

Meteoritics & Planetary Science 1–15 (2015)
doi: 10.1111/maps.12434

Hydrogen and major element concentrations on 433 Eros: Evidence for an L- or LL-chondrite-like surface composition

Patrick N. PEPLOWSKI[1*], David BAZELL[1], Larry G. EVANS[2], John O. GOLDSTEN[1], David J. LAWRENCE[1], and Larry R. NITTLER[3]

[1]The Johns Hopkins University Applied Physics Laboratory, Laurel, Maryland 20723, USA
[2]Computer Sciences Corporation, Lanham-Seabrook, Maryland 20706, USA
[3]Department of Terrestrial Magnetism, Carnegie Institution of Washington, Washington, District of Columbia 20015, USA
[*]Corresponding author. E-mail: patrick.peplowski@jhuapl.edu

(Received 08 September 2014; revision accepted 21 December 2014)

Abstract–A reanalysis of NEAR X-ray/gamma-ray spectrometer (XGRS) data provides robust evidence that the elemental composition of the near-Earth asteroid 433 Eros is consistent with the L and LL ordinary chondrites. These results facilitated the use of the gamma-ray measurements to produce the first in situ measurement of hydrogen concentrations on an asteroid. The measured value, 1100^{+1600}_{-700} ppm, is consistent with hydrogen concentrations measured in L and LL chondrite meteorite falls. Gamma-ray derived abundances of hydrogen and potassium show no evidence for depletion of volatiles relative to ordinary chondrites, suggesting that the sulfur depletion observed in X-ray data is a surficial effect, consistent with a space-weathering origin. The newfound agreement between the X-ray, gamma-ray, and spectral data suggests that the NEAR landing site, a ponded regolith deposit, has an elemental composition that is indistinguishable from the mean surface. This observation argues against a pond formation process that segregates metals from silicates, and instead suggests that the differences observed in reflectance spectra between the ponds and bulk Eros are due to grain size differences resulting from granular sorting of ponded material.

INTRODUCTION

Meteorites provide a repository of primitive solar system material for laboratory analyses on Earth. The insights gained from these investigations shed light on the physical and chemical conditions that prevailed during the era of planetary formation. Of particular importance are the ordinary chondrites (OCs), the most common (79.9%) meteorite fall (Keil et al. 1994) and a frequently used chemical analog for the material that accreted to form the terrestrial planets. Differences in O isotopic ratios between the three OC groups, the H (high Fe), L (low Fe), and LL (low Fe, low metal) chondrites, indicate that they originated from at least three distinct parent bodies (Clayton 1993). Considerable efforts have been devoted to identifying these parent bodies in an attempt to provide context for OC meteorite analyses. These efforts include spacecraft-based observations that carry out detailed investigations that are not possible from Earth.

The first mission dedicated to studying an asteroid was the Near-Earth Asteroid Rendezvous (NEAR) project. A major goal of NEAR was to characterize the elemental and mineralogical composition of its target, the near-Earth asteroid 433 Eros, well enough to determine if it is related to any known meteorite type (Cheng et al. 1997). Specifically, the NEAR project sought to investigate the link between the OCs, the most common meteorites, and the S-type (stony) asteroids, the most common near-Earth asteroid spectral type. NEAR orbited Eros, a $33 \times 13 \times 13$ km S-type asteroid, for one Earth year, after which time the spacecraft landed on the surface. NEAR operated for 2 weeks at its landing site, where it carried out the first in situ measurements from the surface of an asteroid.

NEAR measurements were successful in relating the composition of Eros to the OCs; however, conflicting results from the multi-spectral imager (MSI), near-infrared spectrometer (NSI), and the X-ray/gamma-ray spectrometer (XGRS) prohibited further classification among the LL, L, and H groups (McCoy et al. 2001). We have revisited the NEAR XGRS measurements with the benefit of improved detector response information; updated radiation transport modeling; and insights gained from the analysis of gamma-ray, neutron, and X-ray data sets from the MESSENGER mission to Mercury (Solomon et al. 2007). Our results include revised major element abundances and the first in situ measurement of hydrogen on an asteroid. These new constraints rule out a link between Eros and the H chondrites, and provide compelling evidence that the surface composition of Eros is consistent with the L and LL chondrites.

NEAR X-RAY/GAMMA-RAY SPECTROMETER

The NEAR spacecraft carried an XGRS for measuring the elemental composition of the surface of Eros (Goldsten et al. 1997). Although it was classified as a single instrument, XGRS was in practice two distinct subsystems—an X-ray spectrometer (XRS) and a gamma-ray spectrometer (GRS). The XRS subsystem measured characteristic X-ray emission from the elements Mg, Al, Si, S, Ca, Cr, Mn, Fe, and Ni (Trombka et al. 2000; Nittler et al. 2001; Foley et al. 2006; Lim and Nittler 2009). XRS-derived abundances for these elements indicated that Eros had an OC-like surface composition, but with depleted S content likely due to the loss of moderately volatile elements resulting from space-weathering processes (Kracher and Sears 2005). Fe measurements were consistent with the H chondrites, whereas minor element measurements suggested an LL-chondrite-like composition.

The GRS subsystem was designed to measure element-characteristic gamma-ray emission from Eros resulting from the excitation of nuclei by surface-incident galactic cosmic rays (Goldsten et al. 1997). The GRS failed to measure a significant signal from Eros while NEAR was in orbit (Trombka et al. 2001). Measurements taken on the surface were used to characterize O, Mg, Si, K, and Fe abundances at the landing site (Evans et al. 2001). Those values indicated a surface composition that was generally consistent with the OCs, although the Fe/O ratio was a factor of 2–5 lower than expected. That observation led Evans et al. (2001) to suggest that the NEAR landing site might not be representative of the overall surface composition of Eros. This was notionally supported by the fact that NEAR landed in a ponded regolith deposit (Veverka et al. 2001), material that was hypothesized to be subject to metal/silicate fractionation via nonuniform sorting of regolith grains (Robinson et al. 2001).

REVISITING THE GRS SURFACE MEASUREMENTS

Detector Response

The GRS subsystem consisted of a NaI sensor surrounded by a Bismuth Germanate (BGO) anti-coincidence shield (ACS) for background rejection (Goldsten et al. 1997). The BGO ACS, which surrounded the NaI sensor on all but the asteroid-facing side, was used to veto spacecraft-originating gamma-ray backgrounds while allowing Eros-originating gamma-ray signals to pass unimpeded through the ACS boresight to the NaI sensor. The boresight provided a ~50° full-width half-maximum aperture. Ground-based instrument calibrations were only carried out for the small detector incidence angles (<40°) expected during orbital measurements (Evans et al. 2000), and the NaI detector response at larger angles was modeled using Monte Carlo simulations.

Following the landing of the NEAR spacecraft, the GRS was located just centimeters from the surface with an angle between the instrument boresight and the surface-perpendicular vector of 18°. In this geometry, gamma-ray signals originated from angles ≤108°, a range that is much larger than that characterized during the ground calibration campaign (Evans et al. 2000). In this orientation the asteroid filled the entire FOV of the NaI sensor and ~2π (50%) of the ACS field of view, placing the ACS in a suitable measurement geometry to also provide useful data. The larger size, higher gamma-ray detection efficiency, and largely unobscured view of the surface afforded by the ACS provide excellent measurements of gamma-ray emission from the surface of Eros. Additionally, the NaI measurements were compromised by neutron activation of ^{128}I in the detector, whose beta decay produced a low-energy (<2 MeV) continuum that lowered the signal-to-background for many lines of interest (Evans et al. 2001). For these reasons, we chose to focus our reanalysis efforts on the ACS measurements.

The gamma-ray detection efficiency for the GRS is both energy and incidence-angle dependent (Evans et al. 2000). As no detector efficiency information has been published for the ACS, the use of this data set required the development of a detector response model for the surface measurement geometry. This began with the creation of a GEANT4 (Agostinelli 2003) radiation transport model of the NEAR GRS. GEANT4 was chosen due to its recent use modeling the

MESSENGER GRS detector response, where it successfully reproduced the measured response over a wide range of gamma-ray energies (300 keV–10 MeV) and incidence angles to within 5% of ground-based calibration measurements (Peplowski et al. 2012). The modeled NEAR GRS detector response was benchmarked using new detector efficiency measurements carried out with the NEAR GRS engineering model. The new measurements included a range of incidence angles (0°, 30°, 60°, and 90°) and energies (340, 569, 661, 834, 1067, 1173, 1332, and 1770 keV), providing a robust verification of the GEANT4 model. The model was then used to reproduce the exact geometry of the surface measurement, and to extend the efficiency characterization to energies >2000 keV, which were not included in the calibration campaign.

Spectral Analysis

Elemental abundance information is derived from the summed gamma-ray spectra shown in Fig. 1. The gamma-ray signatures of interest are the peaks located at 846 keV (Fe), 1369 keV (Mg), 1778 keV (Si), 6129 keV (O), and the unresolved doublet consisting of the 7631- and 7646-keV Fe peaks, hereafter referred to as the 7638-keV peak. With the exception of the 7638-keV Fe peak, each signature originates from neutron inelastic-scattering reactions. In this process, a nucleus-incident neutron transfers some of its energy to the nucleus, which temporarily enters an excited state prior to returning to its ground state via the emission of an element-characteristic gamma ray. The 7638-keV peak originates from neutron-capture reactions, whereby the incident neutron is absorbed by the nucleus (^{56}Fe) to create a new isotope (^{57}Fe), which subsequently decays to its ground state via the emission of element-characteristic gamma rays. The distinctions between these two gamma-ray production processes are important during the derivation of elemental weight ratios from the ACS measurements.

For this analysis, we use the summed ACS spectra acquired on the surface of Eros and during the 50-km altitude orbits. The orbit spectrum, which showed no evidence for Eros-originating gamma-ray signatures (Trombka et al. 2001), is used to characterize spacecraft-originating backgrounds following procedures developed during the reduction of MESSENGER GRS data (Evans et al. 2012; Peplowski et al. 2012). Peak areas are derived from each spectrum, and those values are subsequently corrected for the measurement time to produce our measured count rates for each signature (Table 1). The spectral analysis techniques differed depending on the peak of interest. The 846-keV peak areas were determined by fitting a polynomial to the gamma-ray

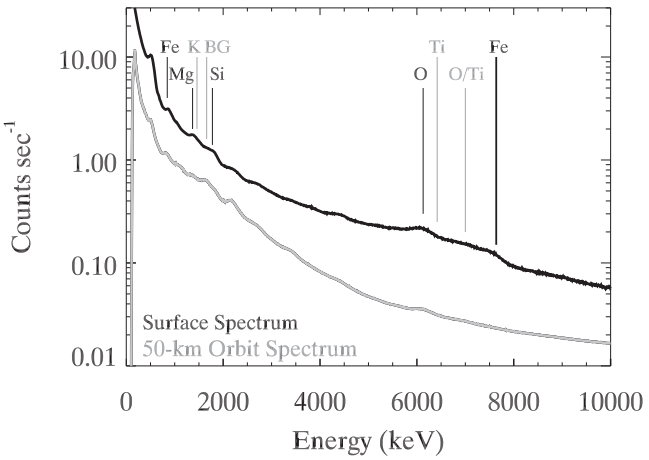

Fig. 1. NEAR Gamma-Ray Spectrometer measurements acquired by the BGO anticoincidence shield on the surface of Eros (black) and during the 50-km orbit (gray). The lack of a signal from Eros during the 50-km orbit facilitates the use of that measurement as a stand-in for the spacecraft backgrounds. Gamma-ray peaks of interest are labeled. Those in gray were not used to derive elemental composition information for Eros for this study. BG is a spacecraft background of unknown origin.

continuum, subtracting it from the spectrum, and summing the residual counts within the peak region of interest. The remaining peaks (1369, 1778, 6129, and 7638 keV) required full spectral fitting to isolate the peaks of interest from neighboring, partially overlapping signals. For example, the 6–8 MeV spectral region required fitting of 6129-keV O, 6419-keV Ti, 6917- + 7117-keV O, and 7638-keV Fe photopeaks along with their first and second escape peaks. Escape peaks, which are found at the full peak energy minus 511 or 1022 keV, result from the escape of annihilation photons from the detector. We left the escape peak fractions (relative to photopeaks) as fitted parameters, finding a probability of 26% for single (511 keV) escape and 4% for double (1022 keV) escape peaks. These values are consistent with results from the GEANT4 simulations.

Background Corrections

The fitted peak areas are dominated by our signals of interest; however, there are contributions from unresolved signatures for each peak. This complication arises from the poor energy resolution of the ACS, which is insufficient to completely resolve the gamma-ray peaks of interest. For instance, the 1778-keV Si peak includes contributions from the unresolved 1809-keV peak, a common detector background signal originating from galactic cosmic-ray excitation and production of Mg. Radiation transporting modeling of gamma-ray production (see the Deriving Elemental

Table 1. Spectral fitting results.

	Energy (keV)	Detection efficiency	Surface[a]		Orbit[b]	Eros flux[c]
			Fitted peak[e] (cps)	Background[f,g] (cps)	Fitted peak[e] (cps)	Counts[f] (cps)
Fe	846	0.61	2.556 ± 0.008	0.49 ± 0.02	0.8235 ± 0.0003	1.74 ± 0.03
Mg	1369	0.52	3.0 ± 0.2	1.04 ± 0.07	1.21 ± 0.05	1.6 ± 0.2
Si	1778	0.46	2.6 ± 0.1	0.76 ± 0.05	1.40 ± 0.06	1.4 ± 0.1
O	6129	0.24	1.87 ± 0.11	0.93 ± 0.04	0.067 ± 0.002	0.9 ± 0.1
Fe	7638[d]	0.21	0.99 ± 0.04	0.11 ± 0.01	–[h]	0.88 ± 0.04

[a]Surface measurement integration time = 346480 s.
[b]Orbit (50 km) measurement integration time = 7944700 s.
[c]Calculated from Equation 2.
[d]Unresolved Fe doublet of 7631- and 7645-keV gamma rays.
[e]Quoted errors are 1 SD statistical errors.
[f]Quoted errors are 2 SD statistical errors and include the systematic error associated with the background corrections.
[g]Derivations of backgrounds is discussed in section Background Corrections.
[h]No high-energy Fe peak was identified in the orbit spectrum.

Abundance Information section for additional details) was used to estimate the contributions of unresolved background signals to our measured peak areas. Our modeled gamma-ray spectra were used to estimate the fraction of each ACS peak that does not originate from the element of interest. This fraction was multiplied by the measured surface count rates to produce an estimated background rate (Table 1), a value that includes an estimate of the statistical uncertainties of the models.

In the case of the 6129-keV O peak, the dominant backgrounds originate from unresolved 5920- and 6018-keV Fe neutron-capture peaks. Instead of relying on the gamma-ray production simulations, we calculate these backgrounds by scaling the measured 7638-keV Fe doublet peak area by the known differences in the intensities (I) of these gamma rays and the relative detector efficiency at the relevant energies as

$$\frac{I_{5920}+I_{6018}}{I_{7631}+I_{7646}}\frac{\varepsilon(6100\text{keV})}{\varepsilon(7600\text{keV})}C_{7638}=0.41\pm0.02\,\text{cps} \quad (1)$$

where the I values for the 5920-, 6018-, 7631-, and 7646-keV Fe gamma-rays are 8.8, 9.1, 26.6, and 22.9, respectively (Reedy and Frankle 2002), the detector efficiency values (ε) at 6100 and 7600 keV are 0.24 and 0.21 (Table 1), and the surface Fe gamma-ray count rate for the 7638-keV doublet (C_{7638}) of 0.99 ± 0.04 counts sec^{-1} (cps; Table 1).

There is an additional source of background that must be removed from the 6129 keV O surface measurement. It is due to Eros-originating neutron excitation of the ACS itself. The ACS is composed of BGO ($Bi_4Ge_3O_{12}$), which has an O number fraction of 0.63. These O nuclei, like those within the surface of Eros, are subject to excitation by high-energy (fast) neutrons and subsequent 6129-keV gamma-ray emission. This background was observed in space, where we measured the 6129-keV count rate to be 0.067 ± 0.002 cps (Table 1). The fast neutron flux present on Eros' surface is significantly larger than that experienced in free space (e.g., the 50 km orbits), therefore the 6129-keV background in the detector will be higher on the surface than in the 50-km orbit.

While radiation transport modeling offers a means of simulating the increase in the 6129-keV background from orbit to the surface measurements, we instead turn to flight data acquired by the MESSENGER neutron spectrometer (MNS; Goldsten et al. 2007). MESSENGER orbits Mercury in a highly elliptical orbit (Solomon et al. 2007), therefore the MNS data provide a means of characterizing fast neutron fluxes as a function of distance from a planetary body. The MNS is a spacecraft-mounted instrument, like the NEAR ACS, and therefore to first order it samples a similar background and signal environment. The MNS-derived fast neutron count rate at high altitudes, equivalent to the NEAR 50-km orbit, is ~2 cps. MNS data, with background subtracted and plotted as a function of solid angle (Lawrence et al. 2013), are used to estimate a signal at the surface of 14 ± 1 cps. Note that MNS measurements went to altitudes of 200 km (solid angle = 31% of 4π) and we have extrapolated to a surface measurement (solid angle = 50% of 4π). The MNS data lead to an estimate of the relative increase in the fast neutron flux from high altitudes to the surface of ([14 ± 1] + 2)/2 = 7.5 ± 0.5. We scale our 50-km orbit 6129-keV count rate by this increase in the fast neutron flux to estimate the ACS background at the surface to be 0.51 ± 0.04 cps. Although this estimate relies on the assumption that the MESSENGER and NEAR neutron fluxes are comparable, we find that our

Si/O versus Mg/O measurements (see the Major Element Measurements section) as well as a comparison of our Fe/O values to those of Evans et al. (2001) (see the Comparison to Previous Measurements section) support the validity of this correction. This background estimate is added to the result of Equation 1 and reported as the total 6129-keV background in Table 1.

Eros-originating gamma-ray count rates (C_E) for each gamma-ray signature of interest are derived from fitted peak and background estimates listed in Table 1 as

$$C_E = C_S - C_B - \frac{C_O}{2}, \quad (2)$$

where C_S is the measured count rate at the surface, C_B is estimated background rate, and C_O is the orbital count rate. C_O values, which are attributed to galactic cosmic-ray (GCR) excitation of spacecraft materials, are divided by two to account for the fact that half of the spacecraft-incident GCR flux is blocked while the spacecraft is on the surface relative to the orbital flux. C_E values and 1 SD statistical errors for each gamma-ray peak of interest are reported in Table 1.

Deriving Elemental Abundance Information

The C_E values for each peak are converted to photon ratios at the detector (R_γ) as:

$$R_\gamma = \frac{C_E(E_{\gamma 1})}{C_E(E_{\gamma 2})}\frac{\varepsilon(E_{\gamma 2})}{\varepsilon(E_{\gamma 1})}, \quad (3)$$

where $E\gamma_1$ and $E\gamma_2$ are the energies of the gamma rays of interest and ε is the energy dependent detection efficiency for each gamma ray. For instance, the Fe/Si photon ratio is calculated by dividing the count rate of the 846-keV Fe peak, $C_E(846)$, by the count rate for the 1778-keV Si peak, $C_E(1778)$, and multiplying by the inverse of the ratio of their detection efficiencies ($\varepsilon[846]/\varepsilon[1778]$)$^{-1}$ to correct for the relative difference in the detection efficiency for these two signals. ε values and Eros-originating gamma-ray count rates are listed in Table 1. Photon ratios of interest are listed in Table 2.

Photon ratios are converted to abundance ratios using conversions derived from radiation transport modeling of GCR-induced gamma-ray production in planetary surfaces. We use the radiation transport modeling code MCNPX (Pelowitz 2005) due to its successful application to previous gamma-ray analyses, including those from the Lunar Prospector (Prettyman et al. 2006), Mars Odyssey (Kim et al. 2006), MESSENGER (Evans et al. 2012), and Dawn (Prettyman et al. 2012) missions. MCNPX-modeled neutron fluxes $N_n(E_n)$ are used in conjunction with the gamma-ray production cross sections $\sigma(E_n)$ of Kim et al. (2006) to derive photon ratios as a function of elemental abundances as:

$$R_\gamma = \frac{Y(E_{\gamma 1})}{Y(E_{\gamma 2})} = \frac{\chi_1 \int_0^\infty N_n(E_n)\sigma_1(E_n)dE_n}{\chi_2 \int_0^\infty N_n(E_n)\sigma_2(E_n)dE_n}\frac{A(E_{\gamma 1})}{A(E_{\gamma 2})} \quad (4)$$

where $Y(E_\gamma)$ is the gamma-ray flux for a gamma ray with energy E_γ, E_n is the neutron energy, χ is the molar fraction for the element of interest, and $A(E_\gamma)$ is the energy dependent probability that a gamma ray with energy E_γ will escape the regolith unscattered and be available, at its full energy, for detection by the ACS. $A(E_\gamma)$ values were calculated using the photon cross section database of Berger et al. (1987).

R_γ values were calculated for a diverse range of planetary materials, including Apollo 11 and 16 soils and regolith breccias (Haskin and Warren 1991), achondrite meteorites from Mars (Shergotty) and Vesta (Sierra de Magé), OCs (H, L, and LL), a high-Fe enstatite (EH) chondrite, and a CH carbonaceous chondrite (Lodders and Fegley 1998). These R_γ values, which are plotted as a function of elemental weight ratios in Fig. 2, were used to derive linear relationships that provided the conversion used to produce the elemental weight ratios from our measured photon ratios. Our reported weight ratios, listed in Table 2, include the 2 SD statistical and systematic uncertainties. In addition to the previously cited systematic uncertainties, the reported values include uncertainties associated with the modeled detector response as well as the photon ratio to abundance ratio conversions. The abundance conversions have an estimated uncertainty of 10% on the basis of the input gamma-ray production cross sections and by comparison to the conversion of Evans et al. (2001). The detector response uncertainties are energy dependent, with widely separated (>2000 keV) peaks being assigned an uncertainty of 10%, and 5% for ratios involving peaks closer in energy. These values were informed by the precision of the simulations used to derive the detector response.

RESULTS

Major Element Measurements

We use the NEAR GRS-derived elemental weight ratios to investigate the relationship between Eros and meteorites. Meteorite compositions are derived from the database of Nittler et al. (2004). We apply a single filter

Table 2. Elemental abundance ratios.

		This study[b]	Evans et al. 2001			
		BGO	BGO	NaI—AC[c]	NaI—1st escape[d]	NaI—2nd escape[e]
Fe(846)/Si(1778)	Photon ratio[f]	0.96 ± 0.22	–	0.65	–	–
	Abundance ratio	1.19 ± 0.30	–	0.8	–	–
Mg (1369)/Si(1778)	Photon ratio[f]	1.05 ± 0.32	–	0.75	–	–
	Abundance ratio	0.84 ± 0.27	–	0.75	–	–
Mg (1369)/O (6129)	Photon ratio[f]	0.81 ± 0.31	–	–	–	–
	Abundance ratio	0.36 ± 0.14	–	–	–	–
Si (1778)/O (6129)	Photon ratio[f]	0.78 ± 0.30	–	–	–	–
	Abundance ratio	0.43 ± 0.17	–	–	–	–
Fe(7638[a])/O(6129)	Photon ratio[f]	1.10 ± 0.32	0.32	0.79	0.43	0.42
	Abundance ratio	0.34 ± 0.15[g]	0.16	0.44	0.27	0.26
Fe(846)/O(6129)	Photon ratio[f]	0.75 ± 0.30	–	–	–	–
	Abundance ratio	0.51 ± 0.21	–	–	–	–
Fe(846)/Fe(7638[a])	Photon ratio[f]	0.68 ± 0.22	–	2.9	–	–

[a]Unresolved Fe doublet of 7631- and 7645-keV gamma rays.
[b]Photon ratios include 2 SD statistical errors and systematic errors resulting from Equation 3. Abundance ratios include these errors, along with additional systematic uncertainties introduced during the conversion from photon ratio to composition ratio.
[c]NaI events without a coincident (background) event in the BGO detector.
[d]NaI events in coincidence with a single 511-keV escape gamma ray in the BGO detector.
[e]NaI events in coincidence with both 511-keV escape gamma rays in the BGO detector.
[f]Note that photon ratios derived from BGO measurements are not directly comparable to those from the NaI, due to the different responses of the detectors. Abundance ratios are comparable for all columns.
[g]Calculated using an assumed hydrogen concentration of 500 ppm, consistent with L- and LL-chondrite falls as well as the hydrogen abundance derived from the Fe photon ratio.

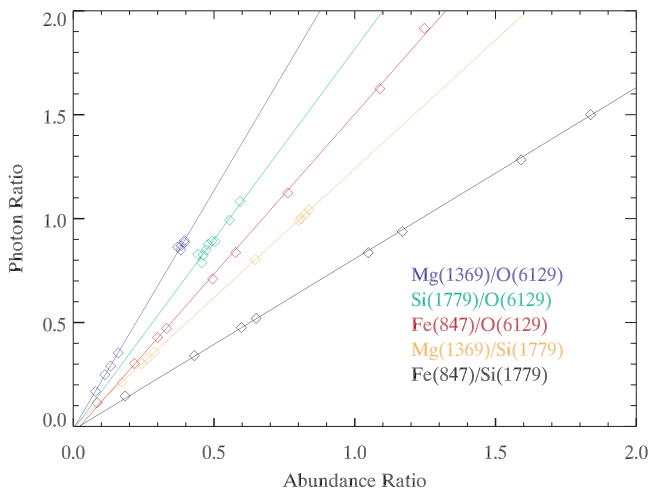

Fig. 2. Modeled relationship between measured photon ratios and elemental weight ratios, color coded by element and gamma-ray signatures. Diamonds denote discrete modeled values for a range of samples, which included ordinary chondrites (LL, L, and H), Apollo lunar soils and regolith breccias (A11 and A16), an HED (cumulate eucrite), SNC (Shergotty), enstatite chondrite (EH), and a carbonaceous chondrite (CH). Lines are linear fits to the modeled data. (see online for color version.)

to the Nittler et al. (2004) values, in which we restrict our comparisons to database entries for which the total elemental composition of the respective meteorite sums to within 1% of 100%, meaning we discard measurements that only quantified a subset of the bulk composition. The remaining ~700 meteorite compositions are plotted in Figs. 3–5. The NEAR measurements, taken from Table 2, are shown as ellipses centered at our measured weight ratios and whose widths represent the 2 SD statistical and systematic uncertainties of the measurements.

Our Mg/Si versus Fe/Si (Fig. 3) and Fe/Si versus Fe/O (Fig. 4) results are each consistent with an L- or LL-chondrite-like composition for Eros, as virtually all of the meteorite compositions (217 samples for L, 78 samples for LL) plotted in Figs. 3 and 4 fall within our measurement ellipses. This contrasts with all other meteorite types, for which either the vast majority of points are outside of the ellipse, or the number of meteorite compositions is too small to draw definitive conclusions. For example, just ~10 out of the 224 H-chondrite meteorite samples plot within the Mg/Si versus Fe/Si measurement ellipse, and just two are allowed by the Fe/Si versus Fe/O measurement. Of the 53 different carbonaceous-chondrite data points, only one (a CV type) falls within our measurement ellipses. Two ureilites and one angrite are allowed by the Fe/Si versus Fe/O measurement, but not the Mg/Si versus Fe/Si result. Finally, one brachinite and most EL enstatite chondrites and acapulcoites are consistent with

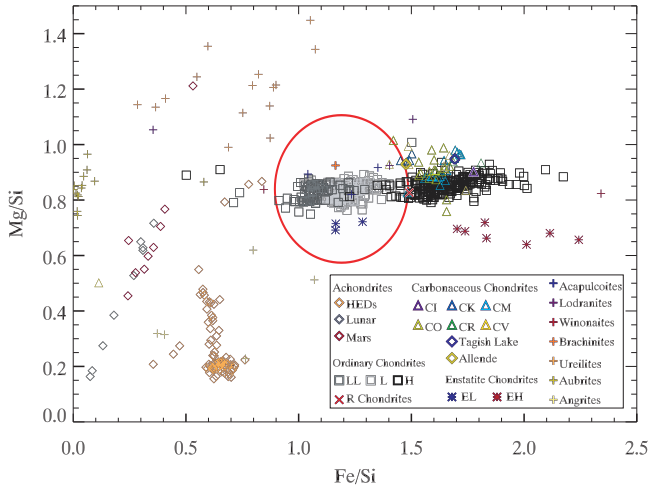

Fig. 3. Mg/Si versus Fe/Si weight ratios for a range of meteorites (see legend) and as measured by the NEAR GRS (red ellipse). The GRS result ellipse includes the 2 SD statistical and systematic errors. The meteorite compositions are derived from the database of Nittler et al. (2004), with the restriction that all plotted values had summed elemental abundances within 1% of unity. (see online for color version.)

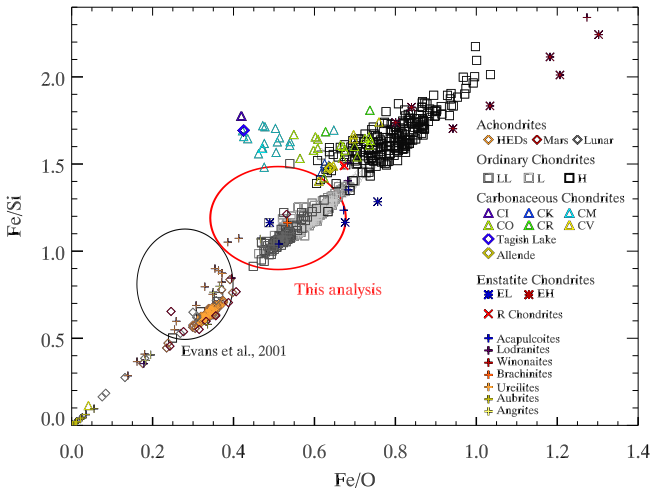

Fig. 4. Fe/Si versus Fe/O weight ratios for a range of meteorites (see legend) and as measured by the NEAR GRS (red ellipse). The GRS result ellipse includes the 2 SD statistical and systematic errors. The meteorite compositions are derived from the database of Nittler et al. (2004), with the restriction that all plotted values had summed elemental abundances within 1% of unity. The Evans et al. (2001) result is also included for comparison. (see online for color version.)

both measurements. Enstatite chondrites can be ruled out by the XRS measurements of Foley et al. (2006) as well as the fact that the silicates in these highly reduced materials are essentially FeO-free and do not exhibit the 1- and 2-μm absorption features that are observed on Eros (Veverka et al. 2000). The brachinites and

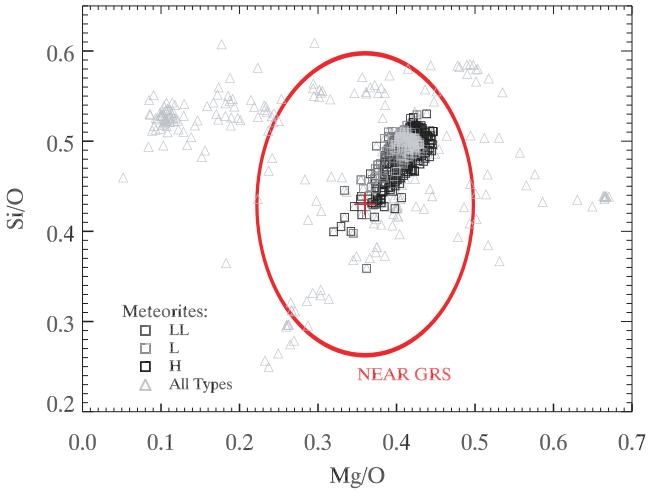

Fig. 5. Si/O versus Mg/O weight ratios for a range of meteorites and as measured by the NEAR GRS (red ellipse). The GRS result ellipse includes the 2 SD statistical and systematic errors. The meteorite compositions are derived from the database of Nittler et al. (2004), with the restriction that all plotted values had summed elemental abundances within 1% of unity. OC meteorite values are represented as squares (see legend), all other meteorites appear as gray triangles. (see online for color version.)

acapulcoites are "primitive achondrites"—meteorites with undifferentiated, chondrite-like composition but textures indicating they have experienced limited melting and melt separation. Although the data sets are limited, these meteorites show a broader range of bulk compositions than chondrites. The chemically distinct lodranites are believed to originate from the same parent body as acapulcoites (e.g., McCoy et al. 2000). The highly uniform mineralogy and composition of Eros derived from NEAR observations thus argues against a connection with the primitive achondrites. We therefore conclude that the revised NEAR GRS measurements strongly indicate that the surface of Eros has an L- or LL-chondrite-like composition.

Unlike Mg/Si versus Fe/Si and Fe/Si versus Fe/O, the Si/O versus Mg/O measurements are not diagnostic of OC subtype. This allows for the use of our Si/O versus Mg/O measurement as a check on our background reduction techniques, particularly those applied to the O signature. Our measured Si/O versus Mg/O value is plotted against meteorite values in Fig. 5, and its close agreement with the OC data cloud, which is centered at Si/O ~0.48 and Mg/O ~0.41, is taken as supporting evidence that our data reduction and background corrections are valid. The agreement between our Fe/O measurements and the O-background-free NaI-AC Fe/O measurement of Evans et al. (2001) also supports this conclusion (see Table 2).

Hydrogen Abundance

Gamma-ray spectroscopy is typically used to characterize hydrogen abundances via measurements of the 2223-keV neutron-capture gamma ray (e.g., Boynton et al. 2002). This signature usually requires hydrogen concentrations of ~0.5 wt% or higher in order to be detectable. Lower hydrogen abundances are typically characterized via neutron spectroscopy (e.g., Feldman et al. 1998a, 2002; Prettyman et al. 2012; Lawrence et al. 2013). NEAR is the only recent spacecraft mission to include a gamma-ray spectrometer but not a neutron spectrometer, and as a result making hydrogen abundance measurements on Eros is difficult given the expected <0.5 wt% hydrogen content of the regolith.

Evans and Squyres (1987) proposed an alternative method for deriving hydrogen concentrations from gamma-ray measurements that is sensitive to low hydrogen concentrations. This technique relies on the fact that there are two reaction mechanisms for producing gamma rays from stable elements. The first mechanism, neutron capture, is most probable with low-energy (<~0.1 eV) neutrons, and as a result neutron-capture gamma-ray fluxes sample the low-energy neutron flux at Eros' surface. The second mechanism, neutron inelastic scattering, requires neutron energies of order 1 MeV or greater for the reaction to occur. As a result, comparisons of neutron-capture- and inelastic-scattering-induced gamma rays provide indirect information on the surface neutron flux. Because the NEAR ACS measurements provide an estimate of Fe photon count rates from both the 846-keV peak resulting from inelastic reactions and the 7638-keV peak resulting from capture reactions, we can apply the Evans and Squyres (1987) methodology to the NEAR data set. While the use of a single element for this study was not strictly necessary, it largely removes any dependence on surface composition, further simplifying the use of these photon ratios to derive hydrogen concentrations for the surface.

Relating our Fe photon ratio to hydrogen content requires the use of our radiation transport models. We produced MCNPX models of the Fe photon ratio for various meteorite compositions, which are plotted versus the macroscopic neutron absorption cross section (Σ_a) in Fig. 6. Σ_a is a measure of the neutron absorption capacity of the near-surface material (e.g., Feldman et al. 1998b; Elphic et al. 2002). Neutron absorbers also modify the Fe gamma-ray ratio by reducing the low-energy neutron flux; therefore, this parameter cannot be neglected. The simulations began with laboratory measured elemental compositions for the selected materials, modified to set the hydrogen content to 10 ppm. Subsequent simulations used hydrogen concentrations that were incrementally increased from

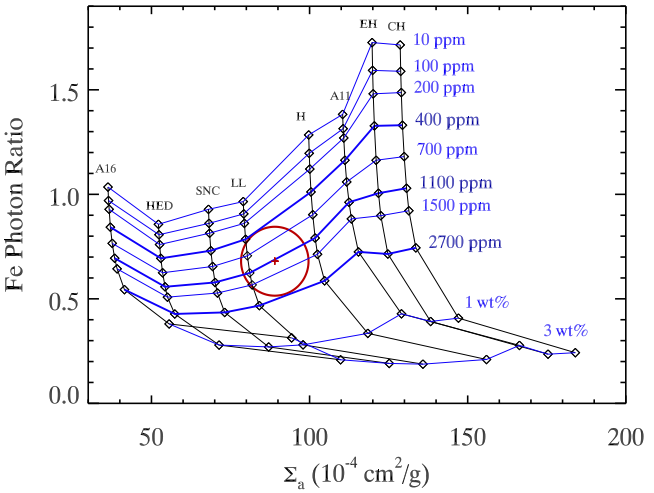

Fig. 6. Modeled Fe photon ratio (847 keV/7638 keV) plotted as a function of macroscopic neutron absorption (Σ_a; see the Hydrogen Abundance section) and varying hydrogen concentrations. Lines of constant hydrogen content are shown as blue contours. Lines of otherwise constant composition, which were calculated for the same reference compositions as Fig. 2, are shown as black contours. The NEAR GRS measured photon ratio is plotted versus the mean Σ_a value for the LL and L chondrites (red cross). The full ellipse includes the 2 SD statistical and systematic errors of the measurement and the 2 SD value of the Σ_a value. (see online for color version.)

10 ppm to 3 wt%. The resulting trend, that for any given meteorite composition the photon flux decreases with increasing hydrogen content, is shown in Fig. 6. This phenomenon is straightforward to understand; increasing hydrogen concentrations moderate more high-energy neutrons to low energies, increasing the availability of neutrons for capture reactions relative to inelastic-scattering reactions and thereby lowering the photon ratio. For any given contour of constant hydrogen, the photon ratio generally increases with increasing Σ_a, reflecting the suppression of the neutron-capture Fe gamma ray due to reduced availability of low-energy neutrons resulting from neutron absorption within the regolith.

The model highlights the fact that, to derive hydrogen concentrations, both the Fe photon ratio and Σ_a value of the regolith must be known. Given that our major element weight ratios strongly support an L- or LL-chondrite-like surface composition for Eros (see Figs. 3 and 4), we use the Nittler et al. (2004) meteorite database to calculate the mean Σ_a value for L and LL chondrites for use in this analysis. The resulting mean, $\Sigma_a = 89 \times 10^{-4}$ cm^2 g^{-1}, and its 2 SD, 11×10^{-4} cm^2 g^{-1}, are combined with our measured photon ratio and its 2 SD uncertainty, 0.68 ± 0.11, to form the error ellipse plotted in Fig. 6. In the context of the model, our measurement lies on the 1100 ppm hydrogen contour, and is fully bounded by hydrogen

contours with 400 to 2700 ppm, leading to our reported hydrogen abundance of 1100^{+1600}_{-700} ppm.

We used the OC chemical measurements of Jarosewich (1990), included in the Nittler et al. (2004) database, to compare our measurement to laboratory derived hydrogen abundances for the L and LL chondrites. This comparison is restricted to considering meteorite falls, which are quickly retrieved samples that are the least likely to contain terrestrial contamination. For LL chondrites, 12 meteorites were used to produce a mean and SD hydrogen concentration of 734 ± 754 ppm. Similarly, 52 L chondrite analyses were used to derive a mean and SD value of 467 ± 464 ppm hydrogen. Figure 7 provides a histogram of these hydrogen values for comparison to the NEAR GRS hydrogen measurement. Our hydrogen abundance is consistent with those of the L and LL chondrites; however, we note that the allowed ranges for both the meteorites and Eros are large and allow for the possibility that the meteorites are depleted in hydrogen relative to Eros.

Eros' measured hydrogen concentration is significantly larger than that found in the lunar highlands, as inferred from the analyses of Apollo 16 samples (~10–110 ppm; Haskin and Warren 1991) and orbital neutron spectroscopy (~20–160 ppm; Lawrence et al. 2014). These hydrogen concentrations are generally attributed to the gradual accumulation of hydrogen via solar-wind implantation over age of the highlands (~4.6 Gyr), a process that should operate similarly on near-Earth asteroids given their similar solar-wind environments. The lunar case therefore provides a benchmark for the total hydrogen accumulation that can be expected from the solar wind, and the significantly higher concentrations found on Eros are likely due to Eros' precursor materials having a higher hydrogen content than the material that accreted to form the Moon.

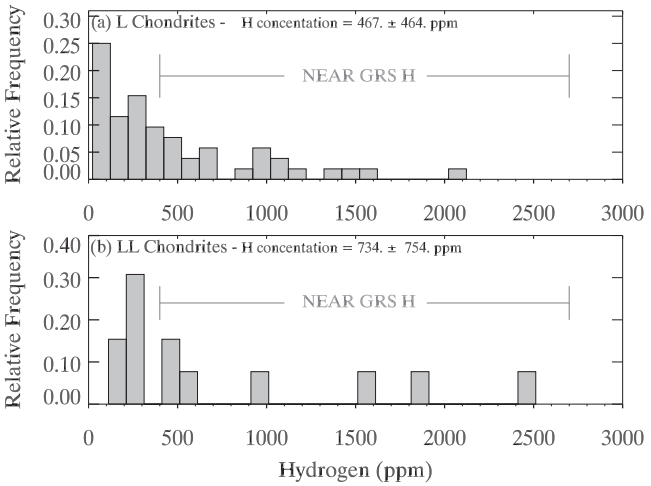

Fig. 7. Laboratory measured hydrogen (H) concentrations measured in observed fall meteorites for a) 52 samples of L and b) 12 samples of LL chondrites. Reported chondrite concentrations represent the mean and 1 SD values of the populations. The GRS-derived H concentration at the NEAR landing site is also shown, and corresponds to the 2 SD range of allowed values.

Comparisons to Previous Investigations

A summary of elemental abundance ratios derived in this study is shown in Table 2, which also includes relevant results from the prior NEAR GRS analysis of Evans et al. (2001). Direct comparisons between the two data sets are complicated by the lack of detailed uncertainties for the Evans et al. (2001) results; however, those authors estimated total uncertainties of ~40%. A number of observations are made during the comparison of these results:

- Our Fe/Si and Mg/Si abundance ratios agree with those of Evans et al. (2001) within the quoted errors of both analyses.
- Our Fe/O ratios, derived using both the 846- and 7638-keV Fe peaks, are consistent with the Evans et al. (2001) NaI-derived values, but not their BGO-derived value.
- Our Fe photon ratio (0.68 ± 0.22) is significantly lower than that of Evans et al. (2001), whose value of 2.9 is unphysical on the basis of our gamma-ray production modeling (Fig. 6).

We consider our 846-keV derived Fe/O abundance ratio to be more robust than 7638-keV-derived values, as it avoids the issue of neutron moderating elements altering the low-energy neutron flux relative to the high-energy neutron flux. The importance of this is shown in Fig. 8, which illustrates the composition- and hydrogen-dependent relationship between the Fe/O photon ratio and abundance ratio. Unlike the photon versus abundance ratios of Fig. 2, which are for neutron inelastic-scattering reactions only, Fig. 8 describes a mixed ratio based on both an inelastic scattering and a neutron-capture reaction. The resulting relationships are nonlinear, unlike those shown in Fig 2, and highlight the difficulties associated with using the 7638-keV Fe gamma ray to derive Fe/O. Additionally, Fig. 8 shows that this relationship is sensitive to the hydrogen content of the soil. In the absence of a hydrogen measurement, Evans et al. (2001) assumed a hydrogen concentration of 50 ppm, which we now know to be well below the actual value of the regolith. The 846-keV Fe signature, which is largely independent of the hydrogen content of the regolith and has a linear Fe/O

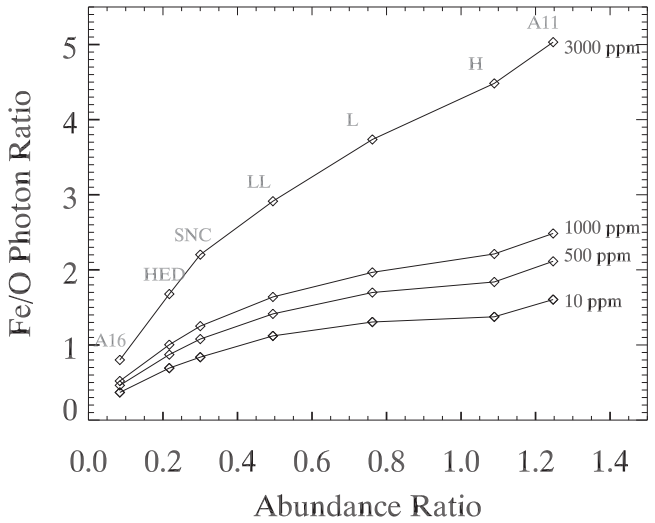

Fig. 8. Modeled Fe/O (7638 keV/6129 keV) photon ratios plotted as a function of Fe/O abundance (weight) ratio for four different assumed hydrogen concentrations. Reference compositions used for these simulations, which are the same used for Fig. 2, are noted in gray.

photon versus abundance ratio, is a less problematic measure for deriving Fe/O weight ratios.

Another likely difference between the Fe/O weight ratio reported here and that of Evans et al. (2001) is the treatment of the 6129-keV O backgrounds. We found that the dominant background to the O gamma-ray peak was intrinsic to the ACS, and therefore by definition this background would be efficiently rejected from the NaI anticoincidence and escape-peak spectra. It is therefore not surprising that the Evans et al. (2001) NaI-derived Fe/O result agrees with our measurement, but that their BGO measurement does not. Because Evans et al. (2001) averaged their four Fe/O measurements, their reported Fe/O abundance was lowered by the BGO measurement, contributing to their finding of a subchondritic value.

Finally, the large differences in the Fe photon flux ratios, which utilized the lowest- and highest-energy gamma-ray peaks reported from NEAR GRS analyses, suggests that the energy-dependent detector response model of Evans et al. (2001) may have been inadequate for comparing widely separated gamma-ray signatures. This hypothesis is supported by the fact that the detector response in the landed geometry was not subject to ground calibrations prior to launch (Evans et al. 2000) and was instead determined from modeling. The impact of a poor detector response model on derived elemental weight ratios varies as a function of the energy difference between the gamma-ray peaks used for each ratio, and in fact for peaks close together in energy we find general agreement with Evans et al. (2001). While the Evans et al. (2001) Fe photon ratio is unphysical on the basis of our modeling, their reported Si photon ratio is allowed by our models. The Si photon ratio used the 1779- and 3539-keV photons, which are much closer in energy and less subject to error resulting from the detector response. We do not report a Si photon ratio because the 3539-keV signature was not observed in the ACS spectra.

REVISITING THE XRS FE/SI MEASUREMENTS

Fe/Si measurements are of particular interest given that Fe is among the most diagnostic elements for discriminating among the H, L, and LL chondrites (see Figs. 3 and 4). The XRS-derived Fe/Si value (1.7 ± 0.3) indicated an H-chondrite-like composition (Lim and Nittler 2009), inconsistent with the revised GRS measurements (Table 2) and the interpretation of MSI/NIS spectra. Okada (2004) suggested that the XRS measurements were compromised by a phase-angle effect, whereby microscopic roughness of the uppermost layer of the regolith alters the measured X-ray emission of the surface at large phase angles. Okada (2004) estimated the magnitude of this effect and concluded that Eros most likely has a lower Fe/Si abundance than previously reported, more consistent with an L- or LL-chondrite-like value. As the phase-angle effect is energy dependent, it was not expected to affect other major element abundances reported from XRS measurements.

Lim and Nittler (2009) attempted to demonstrate and correct this phase-angle effect by defining a path-length parameter that sampled geometric effects. The limited number of measurements and their large errors led them to erroneously conclude that measurement geometry was not influencing the measured Fe/Si abundances. Final confirmation that phase-angle corrections are indeed necessary for deriving Fe/Si abundances came from MESSENGER XRS measurements, which showed a large variation in derived Fe/Si abundances (~0.02 to ~0.09) that are clearly correlated with phase angle (Weider et al. 2014). We therefore conclude that the uncorrected NEAR XRS Fe/Si measurements are not valid constraints on the surface composition of Eros. The most stringent constraints from the XRS therefore come from the minor element analyses of Foley et al. (2006). That analysis found Cr/Fe, Mn/Fe, and Ni/Fe abundances similar to L and LL chondrites, but not H chondrites. The Cr/Fe measurement is particularly robust, given that it is less susceptible to errors in solar modeling and the geometric effects described by Okada (2004). The Cr/Fe measurement was exclusively consistent with the L and LL chondrites.

DISCUSSION

Associating Eros with the L and LL Chondrites

The elemental weight ratios reported here rule out achondrite-, carbonaceous-chondrite-, H-chondrite-, and EH-chondrite-like surface compositions for Eros. An LL- or L-chondrite-like surface composition is robustly consistent with our measurements, although an EL chondrite or other unusual meteorite type (e.g., Acapulcoite, Brachinite) cannot be entirely ruled out (see the Major Element Measurements section). Fortunately, the association of Eros with the LL and L chondrites is supported by prior analyses. Measurements of minor element (Cr, Mn, and Ni) abundances using XRS data produced values consistent with the L and LL chondrites. Lucey et al. (2002) and Clark et al. (2001) used MSI/NSI data sets to characterize the olivine content of the surface and found a best match to the LL chondrites. Similarly, McFadden et al. (2001) examined allowed clinopyroxene and orthopyroxene FeO contents and found a match to LL chondrites, although L chondrites were not strictly excluded. Izenberg et al. (2003) compared NIS- and MSI-derived spectral properties for Eros to those of the OCs, and found a match to the L and LL chondrites.

The aggregate of all NEAR geochemical investigations, and in particular our revised GRS Fe/Si and Fe/O measurements and the recognition that the reported XRS Fe/Si abundances are invalid, provides evidence that Eros has an elemental and mineralogical surface composition that is most consistent with the L and LL chondrites. This introduces the possibility the some of the L or LL chondrites originated from Eros; however, near-Earth asteroids like Eros are not particularly well placed for delivery of ejecta to Earth (e.g., Michel et al. 1999). We suggest that it is more likely that Eros and the L or LL chondrites share a common parent body.

Parent Body of Eros

Eros' geophysical properties also provide constraints on its origin. The density and shape of Eros indicate that it is a consolidated object with an overlying layer of <100-m-thick regolith (Zuber et al. 2000). There is no evidence that it was ever catastrophically disrupted or that it is a rubble pile (Wilkison et al. 2002). The presence of planar fractures are interpreted to have been inherited from its parent, indicating that Eros is a largely intact fragment of a once larger object (Thomas et al. 2002). Dynamical simulations indicate that the lifetime of the orbit of Eros is of order 50–100 Myr (Michel et al. 1998), requiring that it migrated to its present location relatively recently. The likely source region is the Main Asteroid Belt. Bottke et al. (2000) modeled the delivery of near-Earth asteroids from the asteroid belt and found that the most consistent delivery mechanisms were the 3:1 mean motion resonance with Jupiter and the ν_6 secular resonance with Saturn. Dynamical asteroid families located near these resonances are therefore possible sources of near-Earth asteroids like Eros.

Zappala et al. (1997) suggested that the Maria dynamical asteroid family might be the source of the largest near-Earth asteroids, including Eros. The event that disrupted the Maria parent body is expected to have placed a significant number of large fragments into the 3:1 resonance, providing a plausible delivery mechanism. Furthermore, a spectral survey of Maria family members in the 5000–10,000 angstrom range was found to be similar to the corresponding spectrum for Eros (Zappala et al. 1997). Another candidate is the Flora dynamical family, whose members have spectra consistent with the LL chondrites. This asteroid family is located in the inner part of the asteroid belt, near the ν_6 resonance (Vernazza et al. 2008). Dynamical simulations suggest that 40% of all near-Earth asteroids should be delivered via this resonance (Bottke et al. 2002), also making it a probable source of OCs. Whatever the source, cosmic-ray exposure ages of the LL chondrites peak at ~17 Ma, suggesting a possible date for the breakup of the LL chondrite parent body (Marti and Graf 1992). Finally, the Gefion family has been proposed to be the parent body of the L chondrites (Nesvorny et al. 2009). ^{39}Ar-^{40}Ar shock ages suggest that the L chondrite parent body broke up ~470 Myr (Haack et al. 1996; Korochantseva et al. 2007), consistent with increased L chondrite meteorite influxes exhibited by fossil meteorites in Middle Ordovician deposits in Sweden dated to 467.3 ± 1.6 Ma (Schmitz et al. 2001). The estimated olivine fraction for the Gefion family is 62–68% (Nesvorny et al. 2009), consistent with both the L chondrites and the NEAR MSI/NIS data sets (McCoy et al. 2001).

Although there is no precise age determination for the surface of Eros, Clark et al. (2002) provide a very rough age of approximately 2 Gyr. Such an age is clearly inconsistent with the ~17 Ma breakup age of the LL chondrite parent body, leaving the Maria and Gefion families as more likely candidates. However, it is also possible that Eros' parent body is neither asteroid family. Future efforts to identify the parent bodies of the L and LL chondrites may benefit from using the physical and chemical properties of Eros as constraints.

Surface Volatile Depletion

XRS measurements revealed that the sulfur content of the surface of Eros is depleted relative to the ordinary chondrites (Trombka et al. 2000; Nittler et al. 2001). Trombka et al. (2000) proposed two possible explanations for this observation. The first is that the sulfur depletion could be due to limited partial melting of Eros or its parent body, followed by loss of the early S-rich melt. The second is that space-weathering processes have depleted the uppermost surface of volatile species like S (Nittler et al. 2001; Kracher and Sears 2005) while leaving the abundances of other rock-forming elements unaltered. The depth sensitivity of the XRS S measurements is limited to <10 μm and thus cannot be used to evaluate the validity of either hypothesis.

The NEAR GRS measurements, which sample to depths of 10s of cm, provide insights into two additional volatiles species: hydrogen and potassium (K). Evans et al. (2001) reported a K abundance (700 ppm) that is consistent with the OCs. Our hydrogen abundance measurement of 1100^{+1600}_{-700} ppm is also consistent with the L and LL chondrites. Although S is more volatile than K, the lack of depletion in K suggests that the S depletion may simply be a surficial process that would not be reflected in the GRS measurements. This is consistent with the work of Kracher and Sears (2005), who concluded that the S depletion was a surficial (depth <100 μm) phenomenon resulting from space weathering. This conclusion is also supported by the analysis of Foley et al. (2006), who examined minor element abundances (Cr, Mn, and Ni), and concluded that Eros was never subject to partial melting.

The NEAR Landing Site

The final images acquired by NEAR suggest that the spacecraft landed in a ponded regolith deposit (Veverka et al. 2001). Note that the landing site location has been reevaluated since Veverka et al. (2001); however, the properties of the new site are not substantially different than the previous solution (Barnouin et al. 2012). That NEAR landed in an unusual landform raises the possibility that the GRS surface measurements are not representative of the mean surface composition of Eros. Ponds are smooth, flat deposits that have unambiguously distinct color properties that led Robinson et al. (2001) to suggest that they have either unique chemical or mechanical properties. Robinson et al. (2001) suggested that electrostatic migration may play a role in infilling ponds, and because such a mechanism has the potential to operate differently on metal versus silicate grains, Evans et al. (2001) cited this hypothesis as an explanation for the subchondritic Fe/O abundance they derived at the landing site.

Our revised analysis has corrected the GRS-derived Fe/O abundance, finding that the prior low value was likely due to incomplete removal of detector backgrounds. Our new result shows no evidence for metal depletion at the landing site. That our revised elemental measurements indicate an L- and LL-chondrite-like surface composition, identical to conclusions drawn from global MSI/NIS and XRS measurements, indicates that the ponded regolith deposit sampled by the surface measurements does not have a distinct chemical composition relative to the mean surface. This suggests that the pond formation process does not segregate materials by composition (e.g., metal-to-silicate fractionation) and instead argues that the unique color properties of the ponds are due to mechanical properties like grain size or different stages of space weathering. These phenomena would manifest in the MSI/NIS spectra but would not be observed in the GRS measurements.

CONCLUSIONS

We have revisited the NEAR GRS and XRS measurements of the surface composition of 433 Eros. This analysis introduced improvements that were only possible with a new detector response model, as well as lessons learned from the analysis of MESSENGER XRS, GRS, and NS data sets. Specifically, the confirmation of the Fe/Si phase-angle effect for X-rays and measurements of altitude-dependent neutron fluxes for spacecraft-mounted instruments were leveraged to improve the analysis of the NEAR data sets. Our results indicate that the surface of Eros has an L- or LL-chondrite-like surface composition, bringing for the first time agreement between all NEAR geochemical investigations. This also leads to the conclusion that the landing site, a ponded regolith deposit, is compositionally indistinguishable from the mean surface composition. This rules out pond formation hypotheses that result in compositionally distinct materials within the ponded regolith.

We have also carried out the first in situ measurement of the hydrogen concentration on an asteroid. The hydrogen content of the surface of Eros, 1100^{+1600}_{-700} ppm, is consistent with hydrogen concentrations in L- and LL-chondrite falls. Taken together with prior GRS-derived K abundances, we support the hypothesis that the S depletion observed by the XRS is a surficial process resulting from space weathering and not a bulk property of the asteroid. These results argue against S loss due to partial melting

of Eros or its parent body, reaffirming Eros' nature as a primitive, undifferentiated solar system body.

Acknowledgments—This work was funded by the NASA Planetary Mission Data Analysis Program, Grant No. NNX13AQ12G. Additional support was provided by the Volatiles, Regolith, and Thermal Investigations Consortium for Exploration and Science (VORTICES) node of the NASA Solar System Exploration Virtual Institute.

Editorial Handling—Dr. Carle Pieters

REFERENCES

Agostinelli S. and the GEANT4 Collaboration. 2003. GEANT4—A simulation toolkit. *Nuclear Instruments and Methods in Physics Research A* 506: 250–303.

Barnouin O. S., Gaskell R. W., and Ernst C. M. 2012. Revisiting the NEAR-Shoemaker landing site (abstract #6419). Asteroids, Comets, Meteors, 2012, May 16–20, Niigata, Japan. LPI Contribution No. 1667. Houston, Texas: Lunar and Planetary Institute.

Berger M. J, Hubbell J. H., Seltzer S. M., Change J., Coursey J. S., Sukumar R., Zucker D. S., and Olsen K. 1987. XCOM: Photon cross sections on a personal computer. Report NBSIR 87-3597. Gaithersberg, Maryland: National Institute of Standards and Technology.

Bottke W. F., Jedicke R., Morbidelli R. A., Petit J.-M., and Gladman B. 2000. Understanding the distributions of near-Earth asteroids. *Science* 288:2190–2194.

Bottke W. F., Vokrouhlikcy D., Rubincam D. P., and Broz M. 2002. The effect of Yarkovsky thermal forces on the dynamical evolution of asteroids and meteoroids. In *Asteroids III*, edited by Bottke W. F., Cellino A., Paolicchi R., and Binzel R. P. Tucson, Arizona: The University of Arizona Press. pp. 395–408

Boynton W. V., Feldman W. C., Squyres S. W., Prettyman T. H., Brückner J., Evans L. G., Reedy R. C., Starr R., Arnold J. R., Drake D. M., Englert P. A. J., Metzger A. E., Mitrofanov I., Trombka J. I., d'Uston C., Wänke H., Gasnault O., Hamara D. K., Janes D. M., Marcialis R. L., Maurice S., Mikheeva I., Taylor G. J., Tokar R., and Shinohara C. 2002. Distribution of hydrogen in the near surface of Mars: Evidence for subsurface ice deposits. *Science* 297:81–85.

Cheng A. F., Santo A. G., Heeres K. J., Landshof J. A., Farquhar R. W., Gold R. E., and Lee S. C. 1997. Near-Earth asteroid rendezvous: Mission overview. *Journal of Geophysical Research* 102:23,695–23,708.

Clark B., Lucey P., Helfenstein P., Bell J. F. III, Peterson C., Veverka J., Moconnochie T., Robinson M. S., Bussey B., Murchie S. L., Izenberg N. I., and Chapman C. R. 2001. Space weathering on Eros: Constraints from albedo and spectral measurements of Psyche crater. *Meteoritics & Planetary Science* 36:1617–1637.

Clark C. R., Merline W. J., Thomas P. C., Joeseph J., Cheng A. F., and Izenberg N. 2002. Impact history of Eros: Craters and boulders. *Icarus* 155:104–118.

Clayton R. N. 1993. Oxygen isotopes in meteorites. *Annual Review of Earth and Planetary Science* 21:115–149.

Elphic R. C., Lawrence D. J., Feldman W. C., Barraclough B. L., Gasnault O. M., Maurice S., Lucey P. G., Blewett D. T., and Binder A. B. 2002. Lunar Prospector neutron spectrometer constraints on TiO_2. *Journal of Geophysical Research* 107:E45024.

Evans L. G. and Squyres S. W. 1987. Investigation of Martian H_2O and CO_2 via orbital gamma ray spectroscopy. *Journal of Geophysical Research* 92:9153–9167.

Evans L. G., Starr R., Trombka J. I., McClanahan T. P., Bailey S. H., Mikheeva I., Bhangoo J., Bruckner J., and Goldsten J. O. 2000. Calibration of the NEAR gamma-ray spectrometer. *Icarus* 148:95–117.

Evans L. G., Starr R. D., Bruckner J., Reedy R. C., Boynton W. V., Trombka J. I., Goldsten J. O., Masarik J., Nittler L. R., and McCoy T. J. 2001. Elemental composition from gamma-ray spectroscopy of the NEAR-Shoemaker landing site on 433 Eros. *Meteoritics & Planetary Science* 36:1639–1660.

Evans L. G., Peplowski P. N., Rhodes E. A., Lawrence D. J., McCoy T. J., Nittler L. R., Solomon S. C., Sprague A. L., Stockstill-Cahill K. R., Starr R. D., Weider S. Z., Boynton W. V., Hamara D. K., and Goldsten J. O. 2012. Major-element abundances on the surface of Mercury: Results from the MESSENGER gamma-ray spectrometer. *Journal of Geophysical Research* 117:E00L07.

Feldman W. C., Maurice S., Binder A. B., Barraclough B. L., Elphic R. C., and Lawrence D. J. 1998a. Fluxes of fast and epithermal neutrons from Lunar Prospector: Evidence for water ice at the lunar poles. *Science* 281:1496–1500.

Feldman W. C., Barraclough B. L., Maurice S., Elphic R. C., Lawrence D. J., Thomsen D. R., and Binder A. B. 1998b. Major compositional units of the moon: Lunar Prospector thermal and fast neutrons. *Science* 281:1489–1493.

Feldman W. C., Boynton W. V., Tokar R. L., Prettyman T. H., Gasnault O., Squyres S. W., Elphic R. C., Lawrence D. J., Lawson S. L., Maurice S., McKinney G. W., Moore K. R., and Reedy R. C. 2002. Global distribution of neutrons from Mars: Results from Mars Odyssey. *Science* 297:75–78.

Foley C. N., Nittler L. R., McCoy T. J., Lim L. F., Brown M. R. M., Starr R. D., and Trombka J. I. 2006. Minor element evidence that asteroid 433 Eros is a space-weathered ordinary chondrite parent body. *Icarus* 184:338–343.

Goldsten J. O., McNutt R. L. Jr., Gold R. E., Gary S. A., Fiore E., Scheider S. E., Hayes J. R., Trombka J. I., Floyd S. R., Boynton W. V., Bailey S., Bruckner J., Squyres S. W., Evans L. G., Clark P. E., and Starr R. 1997. The X-ray/gamma-ray spectrometer on the Near Earth Asteroid Rendezvous Mission. *Space Science Reviews* 82:169–216.

Goldsten J. O., Rhodes E. A., Boynton W. V., Feldman W. C., Lawrence D. J., Trombka J. I., Smith D. M., Evans L. G., White J., Madden N. W., Berg P. C., Murphy G. A., Gurnee R. S., Strohbehn K., Williams B. D., Schaefer E. D., Monaco C. A., Cork C. P., Del Eckels J., Miller W. O., Burks M. A., Hagler L. B., DeTerresa S. J., and Witte M. C. 2007. The MESSENGER gamma-ray and neutron spectrometer. *Space Science Reviews* 131:339–391.

Haack H., Farinella P., Scott E. R. D., and Keil K. 1996. Meteoritic, asteroidal, and theoretical constraints on the 500 Ma distribution of the L chondrite parent body. *Icarus* 119:182–191.

Haskin L and Warren P. 1991. Lunar chemistry. In *Lunar source book: A user's guide to the Moon*, edited by Heiken G. H., Vaniman D. T., and French B. M. New York: Cambridge University Press. pp. 357–474.

Izenberg N. R., Murchie S. L., Bell J. F. I. I. I., McFadden L. A., Wellnitz D. D., Clark B. E., and Gaffey M. J. 2003. Spectral properties and geologic processes on Eros from combined NEAR NIS and MSI data sets. *Meteoritics & Planetary Science* 38:1053–1077.

Jarosewich E. 1990. Chemical analyses of meteorites: A compilation of stony and iron meteorite analyses. *Meteoritics* 25:323–337.

Keil K., Haack H., and Scott E. R. D. 1994. Catastrophic fragmentation of asteroids: Evidence from meteorites. *Planetary and Space Science* 42:1109–1122.

Kim K., Drake D. M., Reedy R. C., Williams R. M. S., and Boynton W. V. 2006. Theoretical fluxes of gamma rays from the Martian surface. *Journal of Geophysical Research* 111:E03S09.

Korochantseva E. V., Trieloff M., Lorenze C. A., Buykin A. I., Schwartz W. H., Hopp J., and Jessberger E. K. 2007. L-chondrite asteroid breakup tied to Ordovician meteorite shower by multiple isocron ^{40}Ar-^{39}Ar dating. *Meteoritics & Planetary Science* 42:113–130.

Kracher A. and Sears D. W. G. 2005. Space weathering and the low sulfur abundance of Eros. *Icarus* 174:36–45.

Lawrence D. J., Feldman W. C., Goldsten J. O., Maurice S., Peplowski P. N., Anderson B. J., Bazell D., McNutt R. L., Nittler L. R., Prettyman T. H., Rodgers D. J., Solomon S. C., and Weider S. Z. 2013. Evidence for water ice near Mercury's North Pole from MESSENGER neutron spectrometer measurements. *Science* 339:292–295.

Lawrence D. J., Maurice S., Peplowski P. N., and Prettyman T. H. 2014. Bulk hydrogen abundances in the Lunar Highlands: Measurements from orbital neutron data (abstract #1565). Proceedings, 45th Lunar and Planetary Science Conference. CD-ROM.

Lim L. F. and Nittler L. R. 2009. Elemental composition of 433 Eros: New calibration of the NEAR-Shoemaker XRS data. *Icarus* 200:129–146.

Lodders K. and Fegley B. Jr. 1998. *The planetary scientist's companion*. New York: Oxford University Press.

Lucey P. G., Hinrichs J. L., Kelly M., Wellnitz D., Izenberg N., Murchie S., Robinson M., Clark B. E., and Bell J. F. III. 2002. Detection of temperature-dependent spectral variation on the asteroid Eros and new evidence for the presence of an olivine-rich silicate assemblage. *Icarus* 155:181–188.

Marti K. and Graf T. 1992. Cosmic-ray exposure history of the ordinary chondrites. *Annual Review of Earth and Planetary Science* 30:244–268.

McCoy T. J., Nittler L. R., Burbone T. H., Trombka J. I., Clark P. E., and Murphy M. E. 2000. Anatomy of a partially differentiated asteroid: A "NEAR"-sighted view of acapulcoites and lodranites. *Icarus* 148:29–36.

McCoy T. J., Burbine T. H., McFadden L. A., Starr R. D., Gaffey M. J., Nittler L. R., Evans L. G., Izenberg N., Lucey P. G., Trombka J. I., Bell J. F. III, Clark B. E., Clark P. E., Squyres S. W., Chapman C. R., Boynton W. V., and Veverka J. 2001. The composition of 433 Eros: A mineralogical-chemical synthesis. *Meteoritics & Planetary Science* 36:1661–1672.

McFadden L. A., Wellnitz D. D., Schnaubelt M., Gaffey M. J., Bell J. F. III, Clark B. E., Izenberg N., Murchie S., Chapman C. R., and Lucey P. G. 2001. Mineralogical interpretation of reflectance spectra from NEAR NIS low phase flyby. *Meteoritics & Planetary Science* 23:1711–1726.

Michel P., Farinella P., and Froeschle C. 1998. Dynamics of Eros. *The Astrophysical Journal* 116:2023.

Michel P., Gonezi R., Farinella P., and Froeschle C. 1999. Dynamical evolution of 1036 Ganymed, the largest near-earth asteroid. *Astronomy & Astrophysics* 347:711–719.

Nesvorny D., Vokrouhlicky D., Morbidelli A., and Bottke W. F. 2009. Asteroidal source of L chondrite meteorites. *Icarus* 200:698–701.

Nittler L. R., Starr R. D., Lim L., McCoy T. J., Burbine T. H., Reedy R. C., Trombka J. I., Gorenstein P., Squyres S. W., Boynton W. V., McClanahan T. P., Bhangoo J. S., Clark P. E., Murphy M. E., and Killen R. 2001. X-ray fluorescence measurements of the surface elemental composition of asteroid 433 Eros. *Meteoritics & Planetary Science* 36:1673–1695.

Nittler L. R., McCoy T. J., Clark P. E., Murphy M. E., Trombka J. I., and Jarosewich E. 2004. Bulk elemental compositions of meteorites: A guide for interpreting remote sensing geochemical measurements of planets and asteroids. *Antarctic Meteorite Research* 17:231–251.

Okada T. 2004. Particle size effect in X-ray fluorescence at a large phase angle: Important on elemental analysis of Asteroid Eros (433) (abstract #1927). 35th Lunar and Planetary Science Conference. CD-ROM.

Pelowitz D. B., ed. 2005. *MCNPX user's manual, version 2.5.0*. Report LA-UR-94-1817. Los Alamos, New Mexico: Los Alamos National Laboratory. 473 p.

Peplowski P. N., Lawrence D. J., Rhodes E. A., Sprague A. L., McCoy T. J., Denevi B. W., Evans L. G., Head J. W., Nittler L. R., Solomon S. C., Stockstill-Cahill K. R., and Weider S. Z. 2012. Variations on the abundances of potassium and thorium on the surface of Mercury: Results from the MESSENGER gamma-ray spectrometer. *Journal of Geophysical Research* 117:E00L04.

Prettyman T. H., Haggerty J. J., Elphic R. C., Feldman W. C., Lawrence D. J., McKinney G. W., and Vaniman D. T. 2006. Elemental composition of the lunar surface: Analysis of gamma ray spectroscopy data from Lunar Prospector. *Journal of Geophysical Research* 111:E12007.

Prettyman T. H., Mittlefehldt D. W., Yamashita N., Lawrence D. J., Beck A. W., Feldman W. C., McCoy T. J., McSween H. Y., Toplis M. J., Titus T. N., Tricarico P., Reedy R. C., Hendricks J. S., Forni O., Le Corre L., Li J.-Y., Mizzon H., Reddy V., Raymond C. A., and Russell C. T. 2012. Elemental mapping by dawn reveals exogenic H in Vesta's regolith. *Science* 338:242–246.

Reedy R. C. and Frankle S. C. 2002. Prompt gamma rays from radiative capture of thermal neutrons by elements from hydrogen through zinc. *Atomic Data and Nuclear Data Tables* 80:1034.

Robinson M. S., Thomas P. C., Veverka J., Murchie S., and Carcich B. 2001. The nature of ponded deposits on Eros. *Nature* 413:396–400.

Schmitz B., Tassinari M., and Peucker-Ehrenbrink B. 2001. A rain of ordinary chondritic meteorites in the early Ordovician. *Earth and Planetary Science Letters* 194:1–15.

Solomon S. C., McNutt R. L. Jr., Gold R. E., and Domingue D. L. 2007. MESSENGER Mission overview. *Space Science Reviews* 131:3–39.

Thomas P. C., Prockter L., Robinson M., Joseph J., and Veverka J. 2002. Global structure of asteroid 433 Eros. *Geophysical Research Letters* 29:46-1–46-4.

Trombka J. I., Squyres S. W., Bruckner J., Boynton W. V., Reedy R. C., McCoy T. J., Gorenstein P., Evans L. G., Arnold J. R., Starr R. D., Nittler L. R., Murphy M. E., Mikheeva I., McNutt R. L. Jr., McClanahan T. P., McCartney E., Goldsten J. O., Gold R. E., Floyd S. R., Clark P. E., Burbine T. H., Bhangoo J. S., Bailey S. H., and Petaev M. 2000. The elemental composition of 433 Eros: Results of the NEAR-Shoemaker X-ray spectrometer. *Science* 289:2101–2105.

Trombka J. I., Nittler L. R., Starr R. D., Evans L. G., McCoy T. J., Boynton W. V., Burbine T. H., Brückner J., Gorenstein P., Squyres S. W., Reedy R. C., Goldsten J. O., Lim L., Hurley K., Clark P. E., Floyd S. R., McClanahan T. P., McCartney E., Branscomb J., Bhangoo J. S., Mikheeva I., and Murphy M. E. 2001. The NEAR-Shoemaker X-ray/gamma-ray spectrometer experiment: Overview and lessons learned. *Meteoritics & Planetary Science* 36:1605–1616.

Vernazza P., Binzel R. P., Thomas C. A., DeMeo F. E., Bus S. J., Rivkin A. S., and Tokunaga A. T. 2008. Compositional differences between meteorites and near-Earth asteroids. *Nature* 454:858–860.

Veverka J., Robinson M., Thomas P., Murchie S., Bell J. F. III, Izenberg N., Chapman C., Harch A., Bell M., Carcich B., Cheng A., Clark B., Domingue D., Dunham D., Farquhar R., Gaffey M. J., Hawkins E., Joseph J., Kirk R., Li H., Lucey P., Malin M., Martine P., McFadden L., Merline W. J., Miller J. K., Owen W. M. Jr., Peterson C., Prockter L., Waren J., Wellnitz D., Williams B. G., and Yeomans D. K. 2000. NEAR at Eros: Imaging and spectral results. *Science* 289:2088–2097.

Veverka J., Farquhar B., Robinson M., Thomas P., Murchie S., Harch A., Antresian P. G., Chelsey S. R., Miller J. K., Owen W. M. Jr., Williams B. G., Yeomans D., Dunham D., Heyler G., Holdrich M., Nelson R. L., Whittenburg K. E., Ray J. C., Carcich B., Cheng A., Chapman C., Bell J. F. III, Bell M., Bussey B., Clark B., Domingue D., Gaffey M. J., Hawkins E., Izenberg N., Joeseph J., Kirk R., Lucey P., Malin M., McFadden L., Merline W. J., Peterson C., Prockter L., Warren J., and Wellnitz D. 2001. The landing of the NEAR-Shoemaker spacecraft on asteroid 433 Eros. *Nature* 413:390–393.

Weider S. Z., Nittler L. R., Starr R. D., McCoy T. J., and Solomon S. C. 2014. Variations in the abundance of iron on Mercury's surface from MESSENGER X-ray spectrometer observations. *Icarus* 235:170–186.

Wilkison S. L., Robinson M. S., Thomas P. C., Veverka J., McCoy T. J., Murchie S. L., Prockter L. M., and Yeomans D. M. 2002. An estimate of Eros's porosity and implications for internal structure. *Icarus* 155:94–103.

Zappala V., Cellino A., Di Martino M., Migliorini F., and Paolicchi P. 1997. Maria's family: Physical structure and possible implications for the origin of giant NEAs. *Icarus* 129:1–20.

Zuber M. T., Smith D. E., Cheng A. F., Garvin J. B., Aharonson O., Cole T. D., Dunn P. J., Guo Y., Lemoine F. G., Neumann G. A., Rowlands D. D., and Torrence M. H. 2000. The shape of 433 Eros from the NEAR-Shoemaker Laser Rangefinder. *Science* 289: 2097–2101.